

A NEW SLICE-BASED CONCEPT FOR 3D PAPER STRUCTURE ANALYSIS APPLIED TO SPATIAL COATING LAYER FORMATION

*Mario Wiltsche¹, Michael Donoser^{1,2}, Wolfgang Bauer¹
and Horst Bischof²*

¹Institute for Paper, Pulp and Fiber Technology, Graz University of
Technology, Kopernikusgasse 24, 8010 Graz, Austria

²Institute for Computer Graphics and Vision, Graz University of
Technology, Inffeldgasse 16, 8010 Graz, Austria

ABSTRACT

This paper introduces a new concept for digitizing the three dimensional paper structure, based on a fully automated micro-tomy process and light microscopy. The microscope can be moved in all three directions of space with high accuracy in order to be able to digitize large samples with high spatial resolution. All components are controlled by a PC interface which enables an automated digitization process.

The literature concerning 3D analysis of paper structure is reviewed. Non destructive and destructive techniques are compared.

Image analysis algorithms for creation of a detailed digital representation are described. This digital data set is analyzed, to derive characteristics of the paper structure.

As a first example of possible applications the analysis of the 3D coating layer formation is presented. The coating layer is detected by means of image analysis based on a 3D color

segmentation concept. Initial experiments on analyzing coated paper samples prove the applicability of the concept.

The correctness of the implemented sample digitization process and following image analysis was validated.

CONTENTS

1	INTRODUCTION	856
2	RELATED RESEARCH	856
2.1	Non destructive methods	857
2.1.1	Confocal laser scanning microscopy – CLSM	857
2.1.2	X-ray microtomography	858
2.1.3	Magnetic resonance imaging – MRI	860
2.1.4	Ultrasonic microscopy	860
2.2	Destructive methods	861
2.2.1	Sheet splitting	861
2.2.2	Serial sectioning	862
3	NOVEL APPROACH	863
3.1	Key aspects	863
3.2	Sample preparation	864
3.3	Design	864
3.4	Operating sequence	866
3.5	Stitching and aligning	867
3.5.1	Stitching	868
3.5.2	Aligning	870
4	IMAGE ANALYSIS	870
4.1	3D coating layer detection	871
4.1.1	3D color segmentation algorithm	872
4.1.2	Multivariate Gaussian distribution	875
4.1.3	Multivariate outlier detection	877
4.1.4	Bayes classification and Bhattacharyya distance	878
4.2	Calculation of coating thickness	881
4.2.1	Center line determination	882
4.2.2	Measurement of coating thickness	883
4.3	3D Visualization	883
5	RESULTS	884
5.1	Validation	884
5.2	Practical application	889
6	CONCLUSION	892
7	OUTLOOK	892

1 INTRODUCTION

Many physical paper properties are strongly influenced by the spatial distribution of the raw materials in the sheet. Paper consists of a network of fibers, fiber fragments, filler particles and sometimes a coating layer.

Each paper grade has to meet particular requirements depending on its intended use. Therefore specialized paper structures should be designed and hence the analysis of the three dimensional paper structure with high spatial resolution is of high industrial interest.

Due to the constantly growing demands for higher and more uniform paper quality, papermakers have to gain more knowledge of the interrelations between paper structure and paper quality characteristics. For instance printability, strength properties and porosity and their relationship to paper structure hold high optimization potential for the papermaking process.

Two major challenges had to be mastered for the intended purpose. Three dimensional digitization at high resolution and extraction of spatial information by means of advanced image analytical methods.

In section 2 the literature concerning 3D analysis of paper structure is briefly reviewed. Non destructive and destructive techniques are compared.

Section 3 introduces a new concept for digitizing the three dimensional paper structure, based on a fully automated microtomy process and light microscopy.

The analysis of the 3D coating layer formation was developed as a first example of a possible application, it is described in section 4. The three dimensional coating layer formation should allow a better insight into several types of mottling problems, i. e. microgloss and backtrap mottle for coated paper grades. These nonuniformities are related to inhomogeneities in the paper and coating structure. Furthermore the modification of the base paper topography due to the coating process can be studied in future.

Validation results, which prove the usefulness of the novel concept, and first applications on coated industrial paper samples are presented in section 5.

2 RELATED RESEARCH

Numerous research activities have been focused on the development of a technology that extracts spatial structures of fibers, filler pigments and coating layer to build a three dimensional model of a paper sheet.

These technologies have to fulfill two conflicting requirements. First a high spatial resolution is required. The diameter of the fibers is about 10 to 30 μm ,

their length is in the magnitude of millimeters, the particle size of fillers is below $1 \mu\text{m}$. Therefore a resolution of at least $1 \mu\text{m}$ is mandatory to detect all fiber components and important details like fiber morphology parameters accurately. Second a sufficient sample size is needed to get reliable and statistical meaningful results. This requirement originates from the heterogeneity of the paper itself, therefore at least one square centimeter should be analyzed. For every square centimeter of a typical sheet of paper the total number of fibers is 10 000 to 100 000, see RETULAINEN et al. [1]. Thus such a large number of fibers is required to obtain statistically meaningful results.

In principle two main approaches to analyze three dimensional paper structures are applied: non destructive and destructive methods.

2.1 Non destructive methods

Non destructive methods generally do not cause any changes in the sample structure during the inspection process, there are miscellaneous techniques available for three dimensional, non destructive analysis of materials.

In the following sections the applicability of CLSM – confocal laser scanning microscopy, X-ray microtomography, MRI – magnetic resonance imaging and ultrasonic microscopy for 3D analysis of paper materials is discussed.

2.1.1 Confocal laser scanning microscopy – CLSM

A survey of several techniques for multidimensional microscopy in different applications areas such as biology, medical and material science is given in [2].

CLSM – confocal laser scanning microscopy – has been commonly used in qualitative and quantitative analysis of paper structure in recent years. The major feature of the CLSM is its ability of optical sectioning through a sample and obtaining its 3D structure non destructively without any pretreatment.

NANKO et al. [3] were one of the first who described an application of CLSM on paper materials. The structure of interfiber bonding in hand sheets was investigated. Structures of the bonded zone and bonded fibers were characterized. The influences of beating, couching, pressing and drying were explored.

MOSS et al. [4] reported studies of fiber morphology, distribution of fines and surface topography based on CLSM. Three dimensional reconstruction of the paper surface was shown.

AURAN et al. [5] used the CLSM to measure the three dimensional surface

structures of wood containing paper samples. In addition the pore size distribution was estimated.

XU et al. [6, 7] describe a method for analyzing fiber orientation in paper samples based on CLSM. The variation of fiber orientation distribution through the thickness of a paper sample was studied.

The limitation of CLSM is that the signal intensity diminishes rapidly with increasing depth in the sample. The light beam is refracted by the outer fiber layers and particularly by filler pigments. Therefore it is not possible to acquire three dimensional data through the entire thickness of a paper sheet. Another disadvantage is the small sized field of view, which is usually below one square millimeter.

2.1.2 X-ray microtomography

For applications in the field of biology and material sciences X-ray microtomographs with high resolution and small sample dimensions have been developed. These tomographs have also been commonly used in paper research in recent years. In principle there are two different ways of depicting 3D structures based on microtomography – beam absorption or phase contrast.

The most straightforward way to provide the necessary contrast for imaging is by using beam absorption [8, 9]. This is the traditional use of X-ray tomography in medical applications. The necessary contrast for imaging between high density bone regions and low density tissue regions based on absorption is sufficient. Paper fibers are made up of carbohydrates and lignin, which contain only the light elements carbon, oxygen and hydrogen. The weakly absorbing fibers make absorptive contrast unsuitable at higher resolutions of about $1\ \mu\text{m}$.

GOEL et al. [10] have shown the application of absorptive microtomography on paper with a commercial CT scanner. The porosity and specific surface area of commercial liquid packaging board samples were analyzed. The results for porosity showed good agreement with results obtained with mercury intrusion porosimetry. The pixel size was about $2.3\ \mu\text{m}$.

HUANG et al. [11] and RAMASWAMY et al. [12] analyzed the pore structure of different handsheets with absorptive microtomography. These results help to explain differences in liquid and vapor transport through different directions of the paper structure. The pixel size in this case was about $2\ \mu\text{m}$.

GUPTA et al. [13] analyzed numerous 3D structural characteristics – like porosity, specific surface area, tortuosity – of commercial paper and hand sheets based on absorptive microtomography. Results clearly show significant differences between the samples.

AALTOSALMI et al. [14] compared numerical and experimental techniques for analyzing flow in fibrous porous materials. The results computed from the tomographic images obtained with a commercial CT scanner showed agreement with results from other methods.

For materials containing only light elements like paper, phase contrast based X-ray microtomography leads to much better image quality. Phase contrast arises in regions of sharp changes in the refractive index of the sample, such as borders between fibers and pores [15, 16].

Phase contrast can only be obtained when the beam is at least partially spatially coherent. This is the case for X-rays obtained from the third generation of synchrotron sources [15], like at the European Synchrotron Radiation Facility – ESRF – in Grenoble. First demonstrations of the feasibility of phase contrast tomography were reported by RAVEN et al. [17] and SNIGIREV et al. [18] in the mid-1990s.

At the ID 22 MICRO-FID beam line at ESRF a lot of research on paper materials has been done. The effective pixel size can be varied between 0.35 and 2.8 μm , with a field of view changing correspondingly between 0.7 and 5.6 mm [15, 19]. SAMUELSON et al. [8, 9] and HOLMSTAD et al. [20] discuss the application of this technique on paper materials. In order to ensure robust analysis of the 3D fiber network based on this image data, extensive image processing is required to enhance contrast and reduce noise, see ANTOINE et al. [15, 16].

HOLMSTAD et al. [21] reported successful application of absorption mode imaging with the ESRF synchrotron source. A cubic voxel size of 0.7 μm^3 was achieved which allowed quantitative analysis of detailed structural properties.

HOLMSTAD et al. [22] compared 3D data obtained with monochromatic synchrotron radiation in phase contrast mode with a high resolution of about 1 μm with a commercial CT scanner at low resolution of about 5 μm . The results show, that the low resolution images are only suitable for comparative studies. Fundamental research requires high resolution 3D data for accurate measurements. KNACKSTEDT et al. [23] reported similar findings: one data set obtained at a synchrotron facility with high resolution (voxel size 0.35 μm) was compared with another obtained from a commercial CT scanner with low resolution (voxel size 2 μm). These results revealed the particular importance of high resolution images for reliable 3D analysis of paper structure.

The level of detail in the synchrotron images is very impressive. Single fibers can be distinguished easily. This is almost impossible in images which were obtained by absorptive microtomography with commercial CT scanners. In this case spatial resolution and contrast is too low for detailed analysis of the three dimensional fiber network structure.

The challenge of the very high spatial resolution of the synchrotron images is the huge amount of volume data. Therefore just small sample sizes below one square millimeter can be handled by commercial personal computers [20]. A disadvantage of this technique is the requirement of a synchrotron source. Hence this method is far too expensive and therefore not feasible for routine analysis on commercial paper samples.

2.1.3 Magnetic resonance imaging – MRI

MRI – Magnetic resonance imaging – also known as NMR – nuclear magnetic resonance – is well established for visualizing spatial distributions of fluids in all kinds of materials. MRI has been applied to study paper drying and moisture transport in paper [24–28].

LEHMANN et al. [29] describe a method based on MRI to analyze the internal structure in filter media. MRI of the original filter media yields inappropriate image quality. Therefore the pore structure in between the fiber network was filled up with water and a contrast agent to get sufficient image quality. The spatial fiber network was calculated from the negativ pattern of the pore structure. A voxel size of $59 \mu\text{m}^3$ was achieved, which is not suitable for 3D analysis of paper samples.

Due to the low maximum resolution of approximately $10 \mu\text{m}$ [30] MRI is from today's point of view not suitably for three dimensional paper structure analysis.

2.1.4 Ultrasonic microscopy

Another method for acquiring three dimensional data is ultrasonic microscopy which is commonly used in medical and industrial applications. FENSTER and DOWNEY [31] give a review of the state of technology in 3D ultrasonic imaging. Various applications of ultrasonic microscopy in medical diagnostics, industrial control sensors and nondestructive evaluation are discussed in [32].

Most industrial and medical imaging is done at ultrasonic frequencies from 1 to 10 MHz, sometimes frequencies up to 1000 MHz and more are employed. With these high frequencies spatial resolutions below $1 \mu\text{m}$ are attainable [32].

Figure 1 shows the achieved image quality for a SC paper sample and a woodfree coated sample. The measurements were performed at a frequency of 50 MHz and an acoustic velocity of 3000 m/s . The axial resolution towards the paper z direction (ZD) was $60 \mu\text{m}$.

It showed that it is extremely difficult to reconstruct the three dimensional

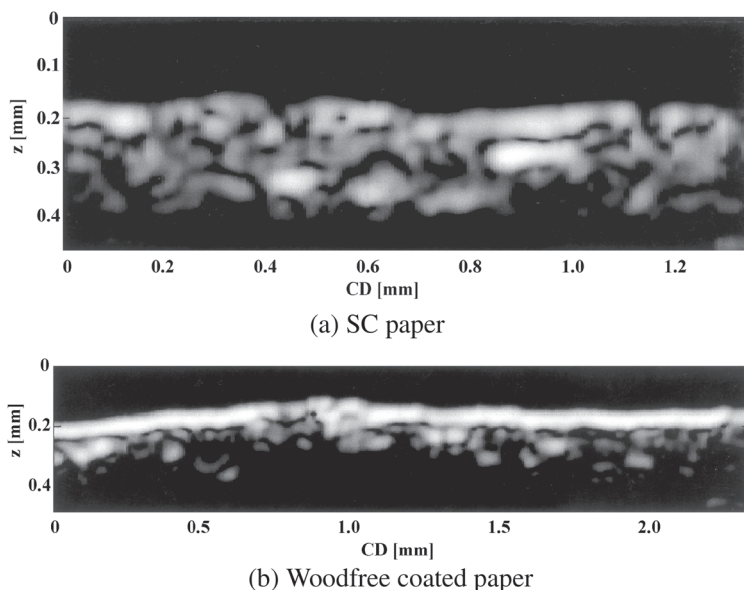


Figure 1 Images obtained with ultrasonic microscopy. Trials were performed at the Institute of Medical Physics and Biophysics, Medical Faculty of the Martin Luther University Halle-Wittenberg in Germany.

paper structure from the data of sound reflections. The attenuation of the ultrasonic waves inside the fiber network of the analyzed samples prevents a total penetration through the entire thickness, this damping occurred in particular in the woodfree coated sample.

Further optimization of this technique is essential to make useful 3D analysis of paper materials, especially a higher resolution and a homogenous analysis of the entire sample thickness are required.

2.2 Destructive methods

The most relevant destructive methods with widespread acceptance for analyzing three dimensional paper structures are sheet splitting and serial sectioning.

2.2.1 Sheet splitting

KNOTZER et al. [33, 34] and HIRN et al. [35, 36] developed a technique in

which samples are split by using a laminating device. With this method it is possible to split a paper sample into very thin layers. An 80 g/m^2 sheet is split in 50 to 100 layers. ERKKILÄ, PAKARINEN and ODELL [37, 38] developed a splitting technique with duct tapes to split paper samples in about 10 layers. THORPE [39] introduced a similar splitting technique to analyze fiber orientation in copy paper. In that case the sample was split into 13 layers.

In these methods the local fiber orientation is determined by means of image analysis in every single layer. The layers are digitally composed to a 3D model of fiber orientation. Using this method local structures in the fiber orientation are made visible, also the local twosidedness of the fiber orientation, which might cause distortions of the sheet, is determined.

The advantage of these splitting techniques is the sample size in the magnitude of several square centimeters. Hence macro effects like cockling or finger-ridging can be explored.

The disadvantages are first the only quasi three dimensional analysis, i.e. it is possible to analyze only the in-plane fiber orientation in every single layer but not the out-of-plane fiber orientation throughout the paper thickness of felted network structures [40]. Second it is impossible to analyze filler and coating layer distribution based on sheet splitting. Furthermore the influence of the splitting process itself on the result is probably considerable.

2.2.2 Serial sectioning

Methods which are based on serial sectioning by a microtome allow a true three dimensional analysis with sufficient resolution and potentially sufficient sample size. In these methods series of vertical cross sections are cut off an embedded paper sample and each section is digitized. Based on these data the three dimensional, internal structure of the sample can be analyzed.

YANG et al. [41] was one of the first who published a method on the basis of serial sectioning. Cut sections were transferred individually on a microscope slide. Single fibers were tracked through the slice images by hand. Hence, the manual work needed was tremendous for even tiny samples. The state of bonding, bonded area, aspect ratios and moments of inertia of fibers were measured.

HASUIKE et al. [42] described a similar method. A $0.2 \times 0.2 \text{ mm}^2$ sized area of a laboratory sheet containing 138 fibers was analyzed. Out-of-plane fiber orientation as well as fiber-to-fiber bonding state were investigated and 3D visualizations of fiber segments were presented.

A combination of sectioning by a microtome and imaging with CLSM is an alternative technique, which is reported by HE et al. [43]. Paper cross sections were imaged with a CLSM inside the embedding mold just below the

cut surface to avoid distortions through the cutting process. The sample size was below one square millimeter, up to 300 fibers were measured inside the paper structure.

In a recent publication ARONSSON [44] discusses slice based digitization of paper. Two different data sets extracted by different approaches are described. The first data set was obtained with a light microscope in transmitted light mode. A rotary microtome was used to cut off thin slices, each of them was placed manually on microscope slides and then stained to enhance contrast. The manipulation of each single slice is a very sophisticated and time consuming process. Distortions or even loss of slices due to cutting and manipulation are unavoidably. These disturbances complicate 3D reconstruction or even make it impossible.

The second data set was obtained with a SEM – scanning electron microscope. Again a rotary microtome was used to cut off thin slices. In this case an image of the cut block surface of the embedded paper sample was acquired. Hence the distortions were much reduced and the 3D reconstruction was more robust.

In both cases the digitization process is very time consuming and extremely laborious. ARONSSON applies an algorithm for segmentation of uncollapsed fibers which appear as ring shaped objects. HAGEN et al. [45] extended this segmentation concept in order to identify even damaged fibers with cracks, which deviate from the ring shaped appearance.

These techniques based on serial sectioning offer the possibility to analyze the three dimensional fiber network structure with high resolution and good image quality. The drawback of these methods is the tremendous effort during the digitization process even for small sized samples.

3 NOVEL APPROACH

3.1 Key aspects

In order to overcome some of the shortcomings of the existing methods a new approach has to fulfil the following requirements in order to allow 3D analysis of larger samples:

- Capability to analyze paper structure in all three dimensions
- Sufficient resolution below 1 micron in image plane
- Sufficient sample size approaching 1 square centimeter
- Low geometric distortion of the sample structure during the digitization process
- Automated process, which enables the digitization of samples within hours
- Possibility for automated image analysis

The presented novel concept is based on automated microtomy and serial sectioning combined with light microscopy. Section 3.2 introduces the sample preparation step, in section 3.3 the design of the automated microtome is described and section 3.4 explains the operating sequence.

3.2 Sample preparation

Sample preparation follows standard embedding procedures which are widespread in microtomy. Different types of molds are used, for instance gelatine capsules with diameter up to 9 mm or histological molds which allow embedding of samples with sizes up to $10 \times 25 \text{ mm}^2$.

Materials used for sample embedding are different types of epoxy resins or glycol methacrylates, the hardness may be varied to suit the particular paper material. The paper samples are dried in a drying oven and after that placed in a case and covered with embedding material. These cases are placed in a desiccator under vacuum for 10 to 120 minutes depending on embedding material and paper grade in order to achieve complete infiltration of the entire sample. In the next step each sample is placed in a separate mold. The mold is then filled with embedding material. Depending on the type of material curing is achieved at room temperature or in an oven at higher temperature of about 60 °C.

3.3 Design

The design consists of a light-optical microscope which is attached to a rotary microtome (see Figure 2). The microtome is used to cut sections with a thickness from 0.5 to 10 μm depending on which type of knife – tungsten carbide, glass or diamond – is used. The microscope is fixed on a stage, which

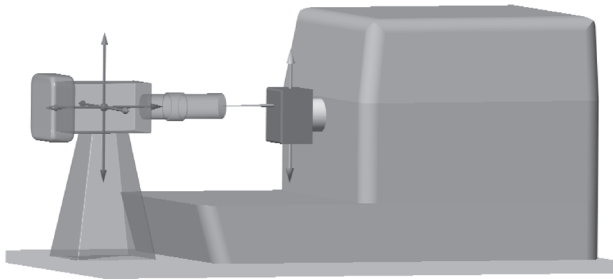


Figure 2 Design of automated microtome. Arrows indicate the three dimensional movability of the microscope and the cutting movement of the rotary microtome.

is placed in front of the microtome and can be moved with high accuracy in all three dimensions. The system is equipped with a CCD camera for digital imaging.

The field-of-view covered by a single image (see Table 1) does not reach the required sample size. Thus, it is necessary to acquire a sequence of adjacent images covering the entire region of interest of the sample.

Generally the samples are embed in a vertical position. After each cut the CD-ZD-plane of the paper sample is imaged, for example see Figure 3. The resolution in MD depends therefore on the slice thickness.

Table 1 Range of achievable resolutions and corresponding fields of view.

Magnification	Pixel size [μm]	Field of view [μm]	
10	1.29	1 681	1 293
20	0.65	841	647
50	0.26	336	259

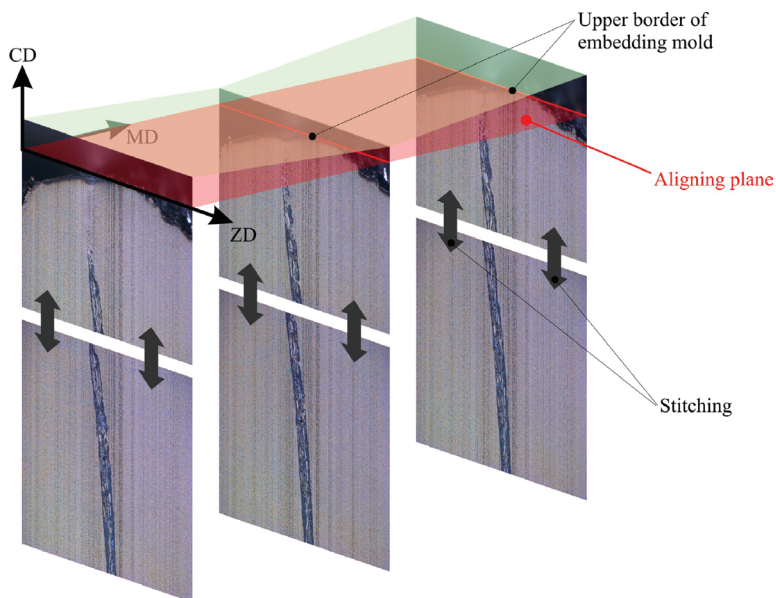


Figure 3 Concept of stitching and aligning. The inclined planes indicate the vertical sample displacements due to the limited positioning accuracy of the rotary microtome after each cut.

3.4 Operating sequence

The microtome, light source, CCD camera and stage are controlled by a PC interface. Repeatedly, slices are cut off the embedded paper sample and the surface is scanned fully automated. Thus the digitization is done on the non distorted surface and thereby guaranties high accuracy between adjacent slices. Furthermore the process is operated without unclamping the embedded paper sample. The sequence consists of the following steps:

- Preparation of the microtome
Trimming of the embedded sample, clamping and touching.
- Setting required parameters
Light intensity, camera settings, auto-focus-settings and region of interest including number of cuts have to be specified.
- Start of the digitization process
Digitization of the entire region of interest can be started with a single mouse click without any further user interaction needed. The program itself triggers the microtome, initiates the correct camera movement and acquires the desired sequence of images according to the following loop:
 - The microtome cuts off the first slice.
 - The previously specified region of interest of the block surface is scanned.
 - The next microtome cut is started.

The digitization of a volume as specified in Table 2 takes for instance 80 minutes, the sequence of images has a data volume of 2.5 gigabytes. The resolution in MD is determined by the slice thickness which is in the range between $0.5 \mu\text{m}$ and $10 \mu\text{m}$. One single cut takes between 10 and 20 seconds, acquisition of images from the block surface after each cut takes between 5 and 20 seconds.

Time need for digitization of one square centimeter with a resolution as defined in Table 2 is expected to be less than 12 hours. Future challenges for digitization of large samples are first to ensure constant image quality over

Table 2 Time need of digitization for a sample with above dimensions: 80 minutes.

	Dimension [μm]	Resolution [μm]
CD	3000	0.65
MD	500	5.0
ZD	sample thickness	0.65

hundreds of cuts and second the handling of the huge amount of data, for one square centimeter more than 100 gigabytes.

3.5 Stitching and aligning

Before the digital three dimensional paper sample structure can be analyzed in detail two different pre-processing steps – stitching and aligning – have to be applied to the set of acquired images.

As mentioned above, the field-of-view covered by a single image does not reach the required sample size. That is why the slice area has to be scanned in a sequence of adjacent images. Due to algorithmic and performance reasons this set of images has to be connected to a single composite image, showing one particular paper slice after one microtome cut. This process is referred to as stitching or mosaicing (section 3.5.1). To ensure that the stitching can be done properly, neighboring images have to overlap each other, see Figure 4.

Another problem to cope with are displacements between the subsequent images slices. This problem has its origin in the limited sample positioning accuracy of the rotary microtome after each cut. To obtain an accurate 3D representation of the paper structure the displacements have to be corrected. This correction step is referred to as aligning, which is described in more detail in section 3.5.2.

Figure 3 illustrates the concept of stitching and aligning applied to the paper slice images.

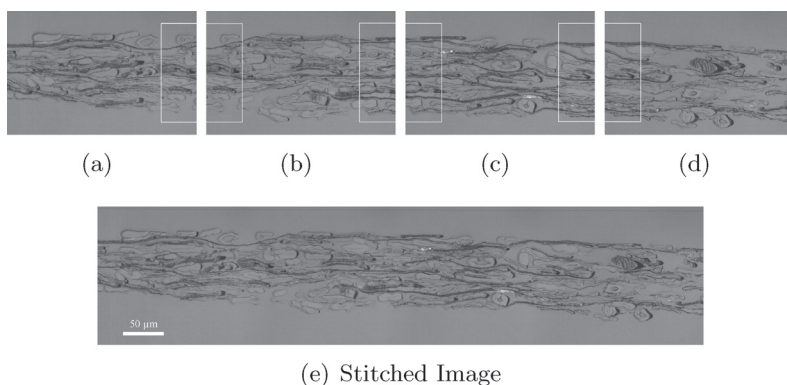


Figure 4 Stitching process applied to 4 paper slice images (anti-clockwise rotated by 90°).

3.5.1 *Stitching*

Stitching (mosaicing) denotes the process of combining several images containing some overlap area into one composite image. It should produce an output image as similar as possible to the input images and the transition between the images should be almost invisible.

Image stitching has been a central issue for a variety of problems in image analysis. It is a well investigated research area, especially due to the success of digital photography and its application area of creating panoramic views [46]. Therefore, most photo programs already provide some simple stitching functionality. Stitching also has its applications in virtual reality [47], 3D model recovery [48] and texture synthesis [49].

BROWN et al. [50] give a comprehensive overview of different stitching concepts. In general image stitching techniques can be classified into two main groups: the direct and the feature based methods. The direct methods use the entire available pixel information to calculate the ideal image registration, whereas feature-based methods first extract points of interest (POI) and afterwards estimate image transformation to find the best registration.

For our work a direct method based on phase correlation [51] was chosen for the correct stitching of the paper slice images.

The images are acquired on the not distorted block surface, instead of the deformed slices. Therefore the general requirements on the stitching process can be simplified based on the following two constraints. First, because the images are acquired from a static scene and the movement of the camera is approximately known, the only transformation, which has to be considered, is translation. Furthermore the overlap between the images is approximately known, because it is manually set by the user during the automated microtomy process. Another simplification is that the sequence of images is arranged column shaped, hence stitching is only made along one border. Image arrangements in matrix form, which require stitching along two borders, are more difficult to perform, but need not to be considered in this particular case.

The stitching algorithm used can be divided into two main steps:

- **Image Registration:** Finding the optimal displacement vector $\mathbf{v} = [\Delta x \ \Delta y]$, representing the searched translational transformation between the images
- **Blending:** Making the transitions between the images almost invisible by applying specific image analysis algorithms

Image Registration – For image registration a method based on phase correlation [51] was chosen: This method is widely used for image registration,

especially due to its exceptional robustness in the presence of noise [52]. Phase correlation uses the frequency domain and exploits the fact that shifts in the spatial domain correspond to linear phase changes in the Fourier domain.

The aim of the image registration step is to calculate a displacement vector $\mathbf{v} = [\Delta x \ \Delta y]$ which best matches one image to another. Thus, by assuming the input of the algorithm are two images named $I_1(x, y)$ and $I_2(x, y)$ the registration problem can be defined as finding those values for Δx and Δy that fulfill Equation (1).

$$I_1(x, y) = I_2(x - \Delta x, y - \Delta y) \quad (1)$$

For further information about the calculation of the displacement vector see DONOSER et al. [53]. REDDY et al. [54] proposed an addition to the phase correlation approach, which considers rotation and scale transformations. But as mentioned before, in our case only translational transformation has to be considered.

Blending – The registration process results in a displacement vector, which is used to stitch the images together. One important property of the final composite image should be that the transitions between the stitched images are almost invisible. This is achieved by another image analysis step called Blending.

There are three main approaches to the problem of Blending, which have been recently used in image analysis [55].

The first approach is to search for a curve in the overlap region on which the differences between the stitched images are minimal [56]. Such an algorithm has the problem that it poorly handles global intensity differences.

The second approach is to use a weighted average of the input images at the overlap region. Such concepts are sometimes referred to as Feathering or Alpha Blending [57].

Pyramid Blending [58] denotes a concept which combines different frequency bands with different alpha masks. The approach produces smooth transitions in lower frequencies while it reduces edge duplication in textured regions. The main problem of this approach is that it poorly handles misalignments.

In our case the second approach, based on weighted averages, was used as Blending algorithm. Therefore new values for the overlap region are calculated by the equation

$$I(i, j) = \alpha_{ij}I_1(i, j) + (1 - \alpha_{ij})I_2(i, j), \quad (2)$$

where $a_{ij} \in [0,1]$ is the weighting parameter and is used to control the blending effect. The values of a_{ij} are set proportionally to the distance to the cutting line. The final result of the three steps

- calculating optimal displacement vector
- stitching the image together based on the displacement information
- applying the Blending algorithm to the overlap region

is a composite image, showing the whole paper slice area after one microtome cut. Figure 4 shows an example for paper slice image stitching.

3.5.2 *Aligning*

Stitching and aligning are two different image analysis problems but they can be solved by very similar algorithms. The main problem for both is to find the displacement that best registers one image with another. Therefore the presented registration algorithm (see section 3.5.1) can also be used for the alignment problem.

Naturally each of the two problems has its own specific requirements. For stitching the registration process can be done accurately, the main focus lies on achieving a very smooth transition between the stitched images. In the aligning process the registration is more difficult, because the scene changes from cut to cut. In contrast to stitching the blending step can be neglected.

In our work aligning is realized by including the upper border of the embedding mold at the top of each slice image, see Figure 3. The contour of the border of the capsule does not change significantly from cut to cut. Thus, the correct alignment can be calculated based on this contour.

After aligning and stitching an accurate digital representation of the paper sample is obtained. As an example Figure 5 shows a small region of a digitized sack paper sample.

4 IMAGE ANALYSIS

After the previously presented processing steps – sample preparation, automated cutting for digitization, stitching and aligning – the final result is a sequence of slice images, which represent the 3D paper structure with a feasible maximum resolution of $0.26 \times 0.26 \times 0.5 \mu\text{m}^3$. This digital representation constitutes the basis for various applications, like e. g. analysis of the coating layer or the fibre network.

Irrespective of the intended application these presented four steps have to be performed in order to ensure a digital representation which is to a high

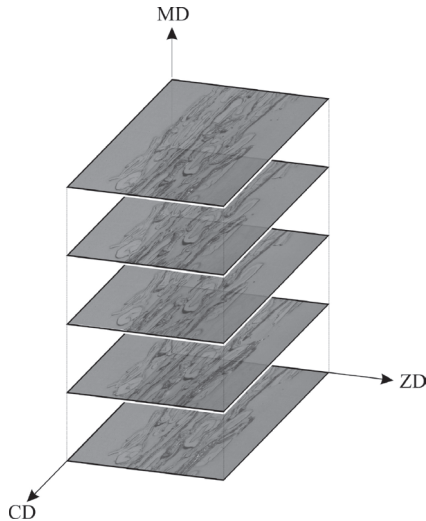


Figure 5 Small cut-out of a digital 3D paper structure representation (kraft paper sample, MD axis not in scale).

degree congruent with the true three dimensional structure of the digitized sample.

4.1 3D coating layer detection

Spatial extraction of coating layer formation was implemented as the first of several possible types of analysis. The coating layer can be identified as the homogeneously colored regions at the surface of the coated paper sample in the slice images. A semi-automatic concept capable of detecting the coating layer in every slice image by a three dimensional color segmentation algorithm was developed and implemented. Section 4.1.1 introduces the segmentation concept in detail, in sections 4.1.2, 4.1.3 and 4.1.4 the required mathematical background is described. Section 4.1.2 shows how a multivariate Gaussian distribution can be fitted to a set of d -dimensional data points. In section 4.1.3 an overview about the concept of detecting outliers in such multivariate distributions is given. Finally section 4.1.4 specifies the main mathematical theory used in this segmentation algorithm, the so-called Bhattacharyya distance and its applications.

4.1.1 3D color segmentation algorithm

One of the most wide-spread techniques to identify and segment regions-of-interest from an image is simple thresholding [59]. For our goal of extracting detailed coating layer information a more complex image analysis approach – a 3D color segmentation concept – has to be applied to achieve suitable results.

One big advantage of the introduced automated microtomy concept is that digital paper structure data is created in all three dimensions. Subsequent slice images, that represent this 3D data, are strongly interrelated. Simple thresholding is only based on 2D image information and does not utilize the advantage of having access to 3D data. Thus, any 3D segmentation approach will lead to significantly better results.

A 3D segmentation approach is also able to even outperform a manual segmentation. For humans it is very difficult to process 3D information for manual segmentation, due to the lack of suitable visualization possibilities of 3D data.

In addition simple thresholding will only classify each pixel for itself, no spatial neighborhood information is included in the classification process. But due to the strong relationship between neighboring pixels of the coating layer, the results will improve a lot, if neighborhood data is included into the decision process.

By using a 3D segmentation approach it is also possible to include the variance of the colors in the neighborhood of a pixel for improvement of classification. Generally thresholding is only applied to grey scale images. Thus, to apply thresholding the color images have to be converted and at this step information is lost.

Summarizing, the three-dimensional color segmentation approach will significantly outperform any thresholding concept by including 3D, variance and color information into the classification process.

The developed segmentation process iterates step-by-step through the sequence of slice images, in order to detect the coating layer in each image and to create a binary output image for each slice. The algorithm is a semi-automatic process, which means that some user-interaction at the beginning of the process is necessary.

A user has to identify the coating layer in the first, and only in the first, slice image. This is done by drawing a free-form-line. Figure 6 shows a slice image and the manually added free-form-line. It has to be pointed out, that only color information is extracted from this free-form-line, all spatial data is neglected. The output of this user-interaction step is a set of color values from the pixels of the free-form-line, using the Red-Green-Blue (RGB) color

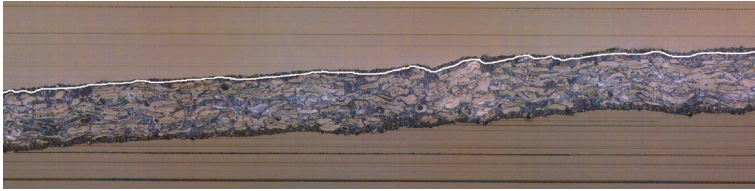


Figure 6 Slice image with manually drawn free-form-line. Only color information is extracted from this free-form-line, all spatial data is neglected.

space for analysis. So each pixel provides color information in terms of three values for the red, green and blue color channel. This color information is used to distinguish the coating layer regions from the rest of the image.

We can assume a Gaussian distribution for the color values of the coating layer, so the first step of the algorithm is to fit such a model to the set of RGB values of the free-form-line. In the case of the RGB feature space a three dimensional Gaussian model is fitted, which is completely defined by nine values, representing the mean vector (three values) and the covariance matrix (six values). In 4.1.2 the general concept behind such a model and how it can be fitted to a sequence of d -dimensional data-points is presented. Afterwards it is necessary to detect and remove outliers in this distribution to make the algorithm more robust (see section 4.1.3), in order to decrease the impact of different free-form-lines.

The next step is to decide for each pixel of the currently analyzed image, whether it is a coating layer pixel or not. Such an assignment process is called classification. In this case only two different output classes have to be distinguished: coating and non-coating. As mentioned before the developed algorithm is a three dimensional algorithm. Thus, the decision if a pixel is classified as coating or not, is based on information originated from the current and the adjacent images. Therefore a 3D kernel, including the neighborhood of the pixel to classify is investigated. The kernel has constant sizes x and y into horizontal and vertical direction within one image and a size z into image sequence direction during the entire segmentation process. So, z describes the number of slice images involved into the classification process. The final size of the kernel is $x \times y \times z$ and can be adapted for various applications. Figure 7 illustrates the three dimensional concept.

As for the pixels of the free-form-line, the current kernel provides another set of pixels with RGB values, e. g. a $5 \times 5 \times 5$ Kernel provides 125 RGB values. As described in section 4.1.2 a multivariate Gaussian distribution can also be fitted to these values.

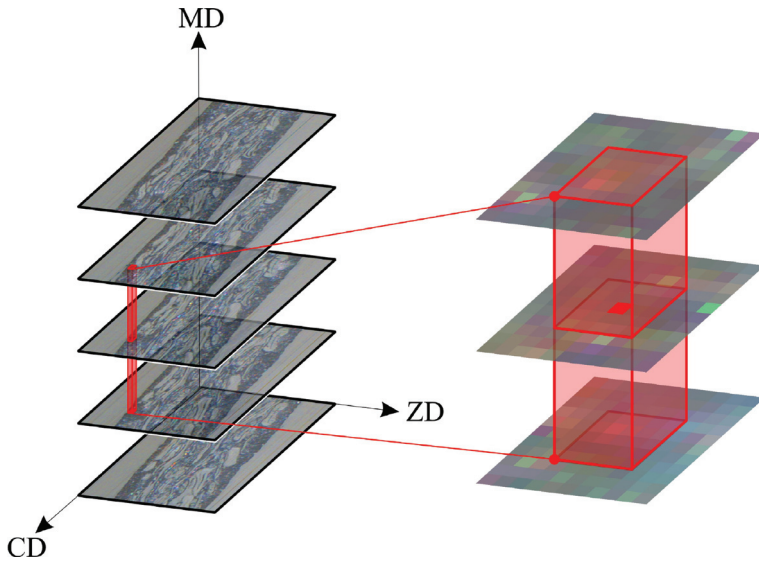


Figure 7 Three dimensional segmentation concept. Analyzed pixel is in the center of the 3D kernel. ($5 \times 5 \times 3$ Kernel with 75 RGB values, MD-axis not in scale).

The final assignment of the currently investigated pixel to one of the two desired output classes (coating / non-coating) is now based on comparing the two estimated multivariate distributions. The first is the one fitted to the RGB color values of the free-form-line and the second one is from the color values of the Kernel around the pixel itself.

The algorithm presented in this paper uses the Bhattacharyya distance [60] to make the decision if the pixel belongs to the coating layer or not. The mathematical background of this distance and required equations are described in section 4.1.4. The comparison of the two multivariate distributions is done by calculating the Bhattacharyya distance, which provides a similarity measurement between the two set of pixels. A fixed distance threshold is used to make the classification. Thus, if the Bhattacharyya distance between the two distributions is smaller or equal than the fixed threshold, the pixel is classified as coating pixel and if the distance is larger the classification results in a pixel assignment to a non-coating region.

This classification step is repeated for every single pixel of the first slice image. Finally, by assigning a 1 to coating-classified pixels and a 0 to non-coating pixels, a binary image, with the coating layer being highlighted, is created, see Figure 8(b).

To continue the classification for all of the slice images, the multivariate Gaussian distribution from the free-form-line of the first image has to be updated for every subsequent slice image, due to possibly changing lighting and color conditions. Therefore the RGB values of all the pixels of the first image which have been assigned to the coating class are collected and the multivariate Gaussian distribution for this set is calculated. Then the presented classification process is repeated for the second slice image, based on this updated distribution.

Finally, every pixel in all of the slice images is uniquely assigned to one of the two classes resulting in a sequence of binary images, in which the coating layer is highlighted. The segmentation result consists of a set of coating regions. The regions which have a size below a fixed threshold are removed. According to experience a threshold of 2 % of the accumulated area of all detected regions leads to meaningful results.

Figure 8 shows a small cut-out of a slice image and the detected coating layer.

4.1.2 Multivariate Gaussian distribution

The general one dimensional Gaussian (Normal) Distribution is defined by the well-known Equation (3). Such a distribution is completely defined by two parameters the mean μ and its variance σ^2 .

$$p(x) = \frac{1}{\sqrt{2\pi}\sigma} e^{-\frac{(x-\mu)^2}{2\sigma^2}} \quad (3)$$



(a) Original image (b) Binary image (c) Combination

Figure 8 Cut-out of a slice image of a coated paper sample.

The Gaussian distribution can be easily adapted to two or more dimensions by matrix notation, whereas the covariance-matrix becomes introduced. The d -dimensional case is written as

$$p(\mathbf{x}) = \frac{1}{(2\pi)^{d/2} |\Sigma|^{1/2}} e^{-\frac{1}{2}(\mathbf{x}-\boldsymbol{\mu})^t \Sigma^{-1}(\mathbf{x}-\boldsymbol{\mu})}. \quad (4)$$

Now \mathbf{x} is a d -dimensional vector, $\boldsymbol{\mu}$ is the d -component mean vector and Σ is the d -dimensional square covariance matrix with d^2 elements. As one can see, for the general d -dimensional case the determination of the covariance matrix and the mean vector completely satisfy to define the model. Figure 9 shows a visualization of a two dimensional Gaussian distribution ($d = 2$).

The covariance matrix contains the variances of the variables x_i in its main diagonal elements named σ_{ii} and the off-diagonal elements σ_{ij} correspond to the covariance of x_i and x_j . If the two variables x_i and x_j are statistically independent the off-diagonal element σ_{ij} is zero. The calculation of the single elements of the covariance matrix is done by Equation (6).

$$\Sigma = \begin{pmatrix} \sigma_{11} & \cdots & \sigma_{1d} \\ \vdots & \ddots & \vdots \\ \sigma_{d1} & \cdots & \sigma_{dd} \end{pmatrix} \quad (5)$$

$$\sigma_{ij} = \mathcal{E} [(x_i - \mu_i)(x_j - \mu_j)] \quad (6)$$

The covariance matrix is always symmetric and positive semidefinite. Due to its symmetry property the d -dimensional covariance matrix can be completely defined by $d(d + 1)/2$ elements.

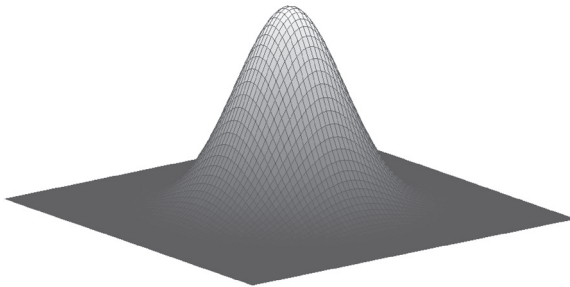


Figure 9 Two dimensional Gaussian distribution.

It is possible to fit such a Gaussian distribution to a d -dimensional data set, by analyzing the data points and calculating the mean vector and the covariance matrix. For any new d -dimensional vector \mathbf{x} it is possible to make a statement about how good it fits into the given Gaussian distribution. The larger the $p(\mathbf{x})$ values becomes the better the vector fits to the model. In practice the entire $p(\mathbf{x})$ is not computed, rather Equation (4) without the normalization term is calculated.

$$\alpha^2 = (\mathbf{x} - \boldsymbol{\mu})^t \boldsymbol{\Sigma}^{-1} (\mathbf{x} - \boldsymbol{\mu}) \tag{7}$$

Equation (7) is called the squared Mahalanobis distance a . Its value measures the distance of the vector \mathbf{x} to the mean vector $\boldsymbol{\mu}$, but corrected for the covariance matrix. For multivariate Gaussian distributions the contours of constant densities are hyperellipsoids of constant Mahalanobis distance to $\boldsymbol{\mu}$. The volume of the hyperellipsoid is a measure for the scatter of the samples around $\boldsymbol{\mu}$. Thus, for the two dimensional case points of equal density lie on an ellipse like illustrated in Figure 10.

4.1.3 Multivariate outlier detection

Outliers in the set of data points can have a significant effect on the fit of the Gaussian distribution. Thus, multivariate outlier detection and removal is necessary to make the algorithm more robust [62].

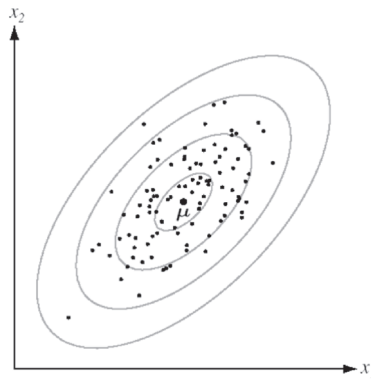


Figure 10 2D Gaussian distribution – pixels with equal Mahalanobis distance lie on an ellipse [61].

An outlier is defined as a data point which is very different from the rest of the data based on a defined criterion, i. e. data which is deviating from the natural data variability. Outliers directly affect means, variances, distortion of estimates and therefore lead to faulty conclusions.

Many multivariate outlier detection algorithms order the data points increasingly by their Mahanalobis-Distance to the estimated Gaussian model and afterwards apply a univariate outlier detection. BARNETT et al. [63] give a comprehensive overview about methods for univariate outlier detection.

An algorithm proposed by ROUSSEUW et al. [64] was implemented. It is based on the fact that for multivariate normally distributed data the values are approximately χ^2 (Chi-Square) distributed with p degrees of freedom. That is the reason why a quantile of the χ^2 distribution (e. g. the 97.5 percent quantile) can be considered as the critical value. Therefore outliers are detected as having a too large Mahanalobis distance compared to the determined critical value.

A more accurate and robust algorithm is the Minimum Covariance Determinant algorithm from ROUSSEUW et al. [65]. This would result in a more robust final mean and covariance estimation, but its computational complexity is high and the benefit of higher accuracy is marginal.

4.1.4 Bayes classification and Bhattacharyya distance

One possibility to do classification is to use the Bayes decision rule. Based on this concept it is possible to unambiguously assign a d -dimensional data vector \mathbf{x} to one of c predefined classes ω_j . Bayes uses a-priori information $P(\omega_j)$ about the probability that a specific class member will appear. In addition class-conditional probability density functions $p(\mathbf{x}/\omega_j)$ are available. This information is afterwards used to convert the a-priori into a posterior knowledge, which constitutes the basis for the class assignment. The corresponding Equation is referred to as the Bayes formula.

$$P(\omega_j/\mathbf{x}) = \frac{p(\mathbf{x}/\omega_j)P(\omega_j)}{p(\mathbf{x})} \quad (8)$$

$$p(\mathbf{x}) = \sum_{j=1}^c p(\mathbf{x}/\omega_j)P(\omega_j) \quad (9)$$

$$posterior = \frac{likelihood \times prior}{evidence} \quad (10)$$

The evidence term $p(\mathbf{x})$ is just a scale factor, which guarantees that the posterior probabilities sum up to 1. So merely the likelihood and the prior term are important for the determination of the posterior probability.

The classification process itself can be represented in different variants. The most popular is to use a set of discriminant functions $g_i(\mathbf{x})$. Thereby the classifier calculates c different discriminant functions and assigns the feature vector \mathbf{x} to a specific class ω_i if

$$g_i(\mathbf{x}) > g_j(\mathbf{x}) \text{ for all } j \neq i. \quad (11)$$

The Bayes decision rule which follows from Equation (8) is to assign a new feature vector x to ω_i if the corresponding posterior probability value is higher as for all the other ω_j .

$$\text{Decide } \omega_i \text{ if } P(\omega_i/\mathbf{x}) > P(\omega_j/\mathbf{x}) \text{ for all } j \neq i \quad (12)$$

In terms of a set of discriminant functions the Bayes classifier formula becomes

$$g_i(\mathbf{x}) = P(\omega_i/\mathbf{x}). \quad (13)$$

Thus, the discriminant functions correspond to the posterior probabilities. The choice of the discriminate function is not unique. $g_i(\mathbf{x})$ can be replaced by any $f(g_i(\mathbf{x}))$, if f is monotonically increasing. The classification result would be the same. Thus another valid representation of Equation (13) is

$$g_i(\mathbf{x}) = \ln p(\mathbf{x}/\omega_i) + \ln P(\omega_i). \quad (14)$$

For the two-category case a single discriminant function can be used instead of two different.

$$g(\mathbf{x}) = g_1(\mathbf{x}) - g_2(\mathbf{x}) \quad (15)$$

Then the algebraic sign of the result can be used as classifier. Therefore, the Bayes Classifier for the two-category case can also be written as

$$g(\mathbf{x}) = \ln \frac{p(\mathbf{x}/\omega_1)}{p(\mathbf{x}/\omega_2)} + \ln \frac{P(\omega_1)}{P(\omega_2)}. \quad (16)$$

For the multi-category case where additionally multivariate normal distributions are assumed,

$$p(\mathbf{x}/\omega_i) \sim \mathcal{N}(\boldsymbol{\mu}_i, \boldsymbol{\Sigma}_i), \quad (17)$$

the Bayes classification rule becomes

$$g_i(\mathbf{x}) = -\frac{1}{2}(\mathbf{x} - \boldsymbol{\mu}_i)^t \boldsymbol{\Sigma}_i^{-1} (\mathbf{x} - \boldsymbol{\mu}_i) - \frac{d}{2} \ln 2\pi - \frac{1}{2} \ln |\boldsymbol{\Sigma}_i| + \ln P(\omega_i). \quad (18)$$

Discriminant functions for some special cases of multivariate Gaussian distributions can be found in [61].

Naturally, the average probability of error which is achieved by Bayes decision rule is from interest. It can be written as

$$P(\text{error}) = \int_{-\infty}^{\infty} P(\text{error}, \mathbf{x}) d\mathbf{x} = \int_{-\infty}^{\infty} P(\text{error}/\mathbf{x}) p(\mathbf{x}) d\mathbf{x}. \quad (19)$$

Thus, if it is ensured that $P(\text{error}/\mathbf{x})$ is as small as possible, the entire integral of Equation 4.1.4 must be as small as possible. By applying the Bayes decision rule of Equation (12) this is guaranteed and so the rule always leads to the lowest average error rate. For the two-category case ($c = 2$) the probability of error becomes

$$P(\text{error}/\mathbf{x}) = \min[P(\omega_1/\mathbf{x}), P(\omega_2/\mathbf{x})]. \quad (20)$$

The exact value of the probability of error is quite difficult to calculate, but in the two-category case the general error integral can be approximated to give an upper bound on the error by Equation (21).

$$P(\text{error}) \leq e^{-k(\beta)} \quad (21)$$

The so-called Chernov bound for $P(\text{error})$ is determined by calculating the value β which minimizes the term $e^{-k(\beta)}$. The Chernov Error Bound is then achieved by setting the calculated β in Equation (21). Finding the value for β which minimizes the whole term can be quite difficult. Thus, in practice the so-called Bhattacharyya bound [60] is used instead. That is the error bound, when β is automatically set to 0.5 without any prior calculation. The Bhattacharyya bound leads to a slightly less tight bound but naturally it is much

$$k(\beta) = \frac{\beta(1-\beta)}{2} (\boldsymbol{\mu}_2 - \boldsymbol{\mu}_1)^t [\beta \boldsymbol{\Sigma}_1 + (1-\beta) \boldsymbol{\Sigma}_2]^{-1} (\boldsymbol{\mu}_2 - \boldsymbol{\mu}_1) + \frac{1}{2} \ln \frac{|\beta \boldsymbol{\Sigma}_1 + (1-\beta) \boldsymbol{\Sigma}_2|}{|\boldsymbol{\Sigma}_1|^\beta |\boldsymbol{\Sigma}_2|^{1-\beta}} \quad (22)$$

easier to calculate. Thus, the final estimate of the maximum error of the Bayes classification process for multivariate Gaussian models, the so-called Bhattacharyya distance, is given by Equation (23).

$$k(1/2) = \frac{1}{8} (\boldsymbol{\mu}_2 - \boldsymbol{\mu}_1)^t \left[\frac{\boldsymbol{\Sigma}_1 + \boldsymbol{\Sigma}_2}{2} \right]^{-1} (\boldsymbol{\mu}_2 - \boldsymbol{\mu}_1) + \frac{1}{2} \ln \frac{\left| \frac{\boldsymbol{\Sigma}_1 + \boldsymbol{\Sigma}_2}{2} \right|}{\sqrt{|\boldsymbol{\Sigma}_1| |\boldsymbol{\Sigma}_2|}} \quad (23)$$

The Bhattacharyya distance provides a quantitative statement about how easily two multivariate distributions can be divided by the Bayes decision rule. That equals to a statement about the similarity of the two distributions. A very high upper bound of error, i. e. a large Bhattacharyya distance, states that it is very difficult to divide the distributions, hence they are very similar. A low upper bound of error, states that the division can be easily made and the distributions are likely to be different. Thus for the two color distributions the Bhattacharyya distance constitutes the basis for a quantitative statement, if the color distributions are likely to be equal or not.

4.2 Calculation of coating thickness

The final output of the three dimensional color segmentation concept presented in section 4.1.1 is a sequence of binary images, wherein the segmented coating layer is highlighted. The next step is to measure the coating thickness on equally spaced positions along the paper surface. Therefore it is necessary to measure the depth of the coating layer in the single binary images.

This measurement is realized in two steps. First, a center line is determined in each of the binary slice images (section 4.2.1). Afterwards the coating thickness is measured by counting pixels along equidistant normals to the center line (section 4.2.2).

The output of this process is a set of distance values, which represent the coating thickness information of the paper sample. Simultaneously information about the base paper topography under the coating layer, as well as the coating surface topography and total paper thickness is obtained. These values can be used to calculate standard parameters like average values, variability and the portion of the coating layer to the entire paper volume. In

addition the extracted spatial coating layer information can also be analyzed with more advanced texture description methods like Wavelets [66, 67] or Fractal analysis [68, 69].

4.2.1 Center line determination

For detection of the center line an image analysis algorithm called skeletonization [70] is applied to a binary image showing the paper cross section.

The skeleton of a region is defined via the medial axis transformation (MAT). The MAT of a region is the set of pixel, which is extracted by following algorithm. For each pixel p of the region the closest neighbor of p on the border of the region is determined. If there exist more than one such border pixel, meaning pixel p has the same distance to a border pixel b_1 and to another border pixel b_2 , then p belongs to the skeleton of the region.

One problem of the skeletonization is that it often produces short extraneous spurs. The removal of this spurs is done in another process called pruning [70]. The method iteratively identifies and removes endpoints from the skeleton, until exactly two remain.

The determined center line constitutes the basis for the measurement lines as can be seen in Figure 11. Possible local changes in its orientation can have an tremendous effect on the orientation of these lines. Therefore the center line has to be smoothed. A moving average of the neighboring coordinates of the center line is finally taken. The order of smoothing can be parameterized to adapt to different kinds of paper surfaces.

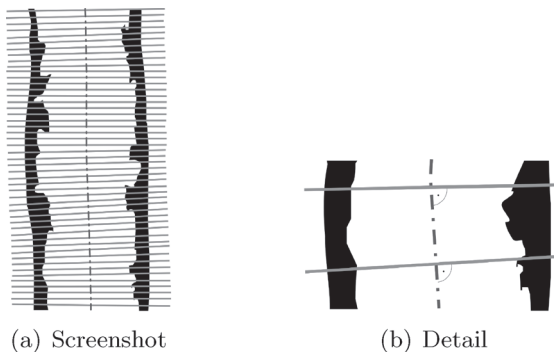


Figure 11 Measurement of coating thickness along normals to the center line.

4.2.2 Measurement of coating thickness

For the measurement of the coating thickness at defined locations on the paper surface, measurement lines are theoretically drawn to each of the binary coating images. These measurement lines are placed orthog-onally on the center line in constant distances Δl . The parameter Δl can be manually adjusted to specify the resolution of the measurement grid. Figure 11 shows a calculated center line and the corresponding perpendicular measurement lines.

Distances are measured on the perpendicular lines, which is done by counting the number of pixels along these lines. The calculation of thickness values is done for each line in the image (m lines) and for all of the slice images (n images). These distances, which are determined in terms of number of pixels can directly be converted to a distance in microns, based on Table 1.

4.3 3D Visualization

The extracted coating layer information is visualized three dimensionally in order to gain detailed insight into data. Interactive tools support exploration of 3D data, for instance a detailed analysis of local defects in a coating layer.

Figure 12 shows a visualization based on the measured coating thickness values of a calendered woodfree coated sample.

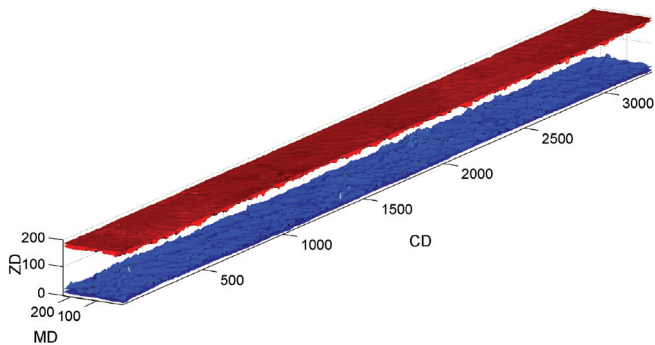


Figure 12 3D visualization of measured coating layer thickness. Axes scale in μm .

5 RESULTS

5.1 Validation

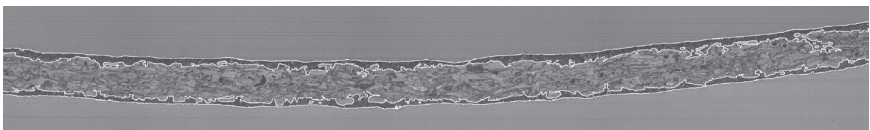
For testing of the robustness of the developed image analysis software, six paper experts drew a free-form-line into an example slice image, as seen in Figure 6. Afterwards the coating detection algorithm was applied to the six created free-form-lines and the results were compared. For this experiment the percentage of pixels which are always classified to the same class is 99.9785 %, which proves the robustness of the concept. The impact of differently drawn free-form-lines is negligible.

The effect of kernel size on the segmentation result was analyzed for all possible combinations between $3 \times 3 \times 3$ and $9 \times 9 \times 9$. Figure 13 shows the effect of the smallest and the largest kernel.

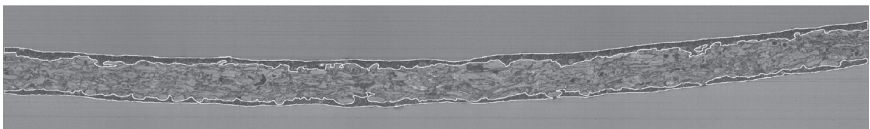
Small kernels tend to segment fine details of the inner coating layer boundary, on the other hand due to their high sensitivity several small regions are misclassified. In contrast large kernels have a strong smoothing effect and therefore some coating layer details are not identified. The advantage of the stronger smoothing is that image noise artifacts are compensated.

The experiments revealed that a kernel size in the range between five and seven yields the best results. Hence, all further coating segmentation results are based on a kernel size of $7 \times 7 \times 7$.

In the next step of validation the paper topography extracted by our prototype was compared with laser profilometric methods [71]. Wood-free coated paper samples with blade-streaks were studied. The spatial topography of the streaks was measured first with a laser profilometer. After that the previously



(a) $3 \times 3 \times 3$



(b) $9 \times 9 \times 9$

Figure 13 Effect of kernel size.

measured region of the sample was embedded and digitized with the presented automated microtomy method.

In Table 3 the level of resolution in different directions in space are summarized for the two methods.

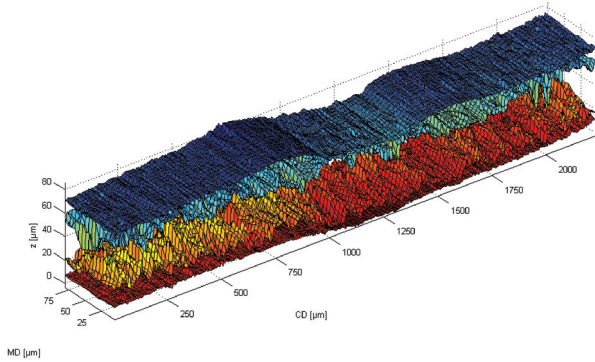
Figure 14 show the 3D visualization of the streak obtained with the two different methods. Table 4 summarizes the corresponding dimensions.

These results showed good agreement between the streak-dimensions measured with laser profilometer and the dimensions obtained with automated microtomy. There are two reasons for the deviations between the methods. First the scratch dimensions are not stable along MD and second the lower resolution of the laser profilometer affected the measurement of the width. These results proved that all of the critical steps in the process chain work accurately. The presented sample preparation ensures a sufficient quality of the acquired slice images in order to identify all paper components of interest. Thus, the need for human assistance at the digitalization step is as low as possible. The stitching and aligning algorithms operate successfully, because small errors in the registration would result in observable disturbances e. g. in the 3D visualizations. Also the coating layer detection and the measurement of its thickness works as the comparison of the metric measurements of the blade-streak demonstrates.

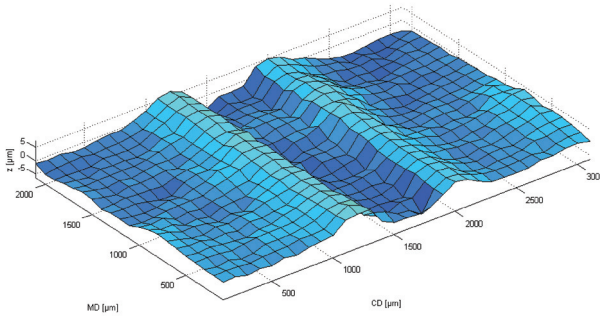
Further validation was done by means of comparing results with a method described in [72] which is applied by IMERYS Minerals Ltd., these results are labeled with "Reference". Samples were embedded and cut in a microtome, the cut surface of the block was imaged with a light microscope. All image data for this comparison was acquired at the identical cut surface of the embedded samples with a cut length of 7 mm. For this purpose the three dimensional coating layer segmentation algorithm described in section 4.1.1 was reduced to 2 dimensions. Two MWC samples were analyzed, Table 5 summarizes the mean values obtained for one of the samples with the two different methods, the following four Figures 15 to 18 show distributions of measured values for basepaper and total sheet caliper as well as coating thickness values on top side and bottom side. These histograms show high similarity regarding mean, variance and shape. The difference in

Table 3 Different resolutions of the compared techniques.

Resolution [μm]	CD	MD	ZD
UBM Laserprofilometer	100	100	$\ll 0.1$
Automated Microtomy	0.65	5	0.65



(a) Automated Microtomy



(b) Laser profilometer

Figure 14 Coating layer with blade-streak.

Table 4 Comparison of results.

Dimensions [μm]	Laser profilometer	Microtomy
Depth Left Edge	8.3	7.4
Depth Right Edge	10.1	10.5
Width between top of edges	815	840
Width of valley	420	450

the class width can be explained by the different pixel sizes of the two methods ($0.5 \mu\text{m}$ for Reference and $0.65 \mu\text{m}$ for the automated microtomy concept).

Table 5 Comparison of mean values.

$[\mu\text{m}]$	Mean Reference	Mean Automated Microtomy
Basepaper caliper	38.3	38.8
Total caliper	53.4	54.2
Top side coating	7.8	8.0
Bottom side coating	7.3	7.5

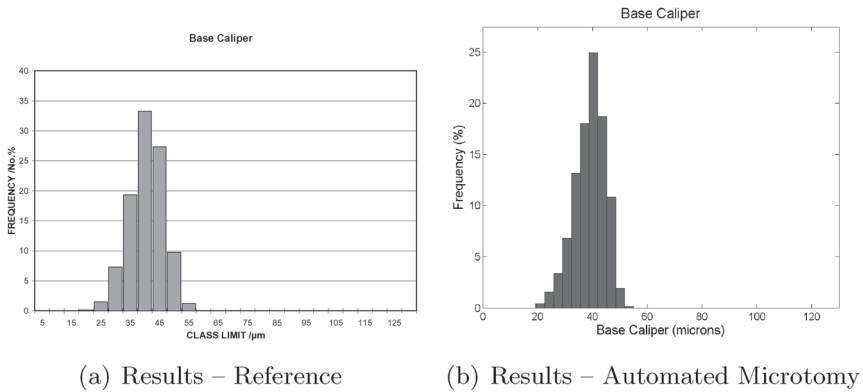


Figure 15 Comparison of basepaper caliper.

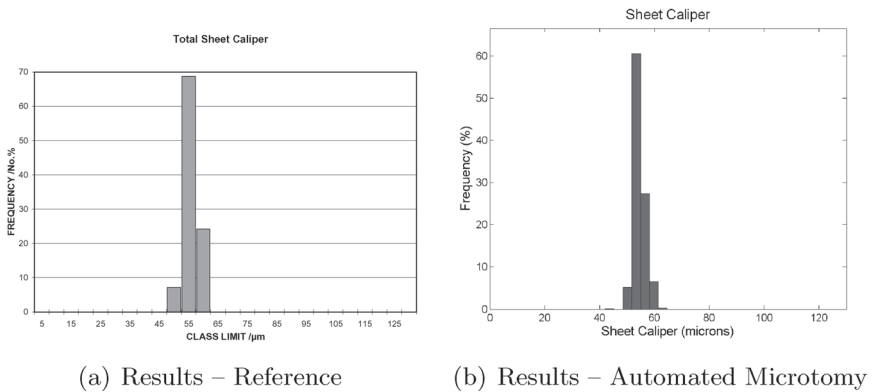


Figure 16 Comparison of total sheet caliper.

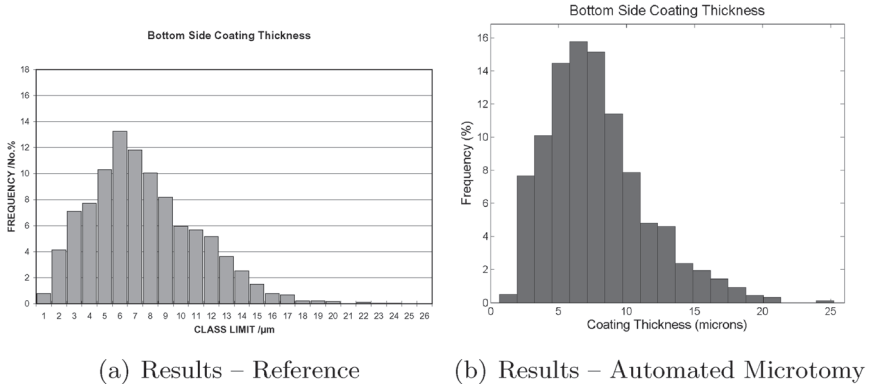


Figure 17 Comparison of coating thickness distribution on bottom side.

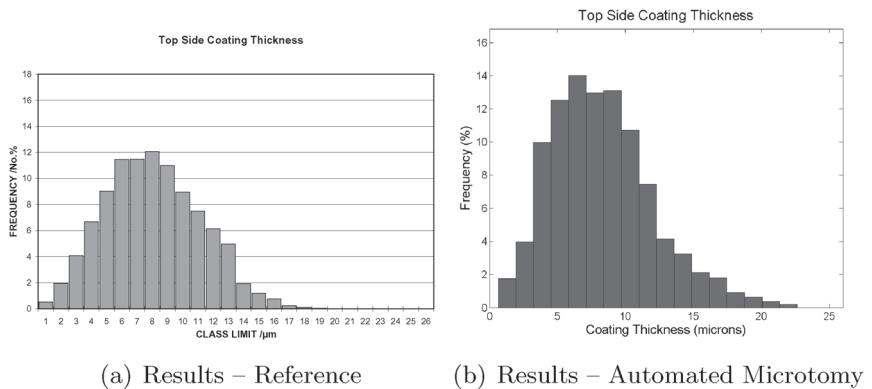


Figure 18 Comparison of coating thickness distribution on top side.

Altogether both methods give similar results if the same cut is analyzed and a high agreement between the two techniques in the respective distributions can be observed. It has to be pointed out again that in case of the results obtained with our novel technique no operator is required to manually detect the coating layer. The only required user interaction is the drawing of the free-form-line, see section 4.1.1.

5.2 Practical application

Initial studies were carried out on comparison of coating layer formation for different pilot scale coating applicators, such as blade, filmpress and curtain coater. Filmpress precoated woodfree base paper rolls (precoat application 9 g/m^2 per side) from a commercial papermachine were top-coated on a pilot coater. The application of the topcoat was performed with filmpress, curtain coater or blade coater. Samples were analyzed before calendering.

The surface of the curtain coated sample shows circular defects, presumably due to air bubbles, see Figure 19, which also affect the local coating thickness, see Figure 20(c).

In Figure 20 the local coating thickness distributions are shown. As expected the blade coated sample shows the most heterogenous coating layer formation, whereas the filmpress and especially the curtain coated samples showed a more uniform coating layer thickness, as would be anticipated for a contour coat. Fibers near the surface of the base paper cause impressions in the coating layer affecting the local coating thickness.

Further studies of different pilot scale coating applicators were carried out on mechanical coated samples. Blade and curtain coated samples were analyzed before and after calendering. Figures 21 and 22 summarize the results for the calendered samples.

The coating thickness distributions of the blade coated samples are wider and the total sheet caliper is more homogenous compared to the curtain coated samples. The distributions of the basepaper caliper under the coating layer are similar for the two samples. Similar findings were obtained for the uncalendered samples.

In the same manner the calendering effect was studied for these samples. Calendering primarily affects the distribution of the basepaper caliper and in

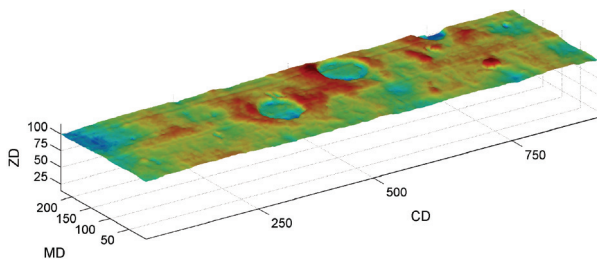
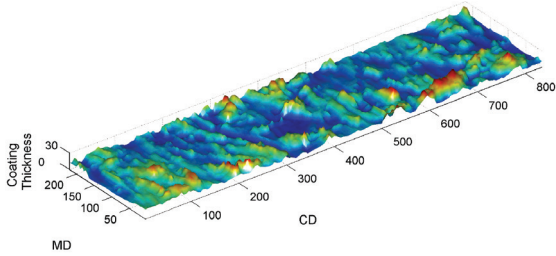
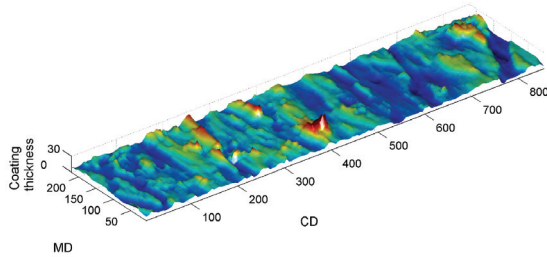


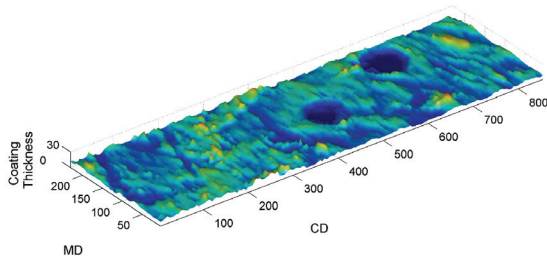
Figure 19 Defects in curtain coated sample. Axes scale in μm .



(a) Blade coater (Filmpress precoated)



(b) Filmpress (Filmpress precoated)



(c) Curtain coater (Filmpress precoated)

Figure 20 Coating thickness compared from different coating applicators. Axes scale in μm .

direct consequence the distribution of the total sheet caliper. Especially the total sheet caliper is noticeably more homogenous after calendering. The coating thickness distributions remained almost unchanged.

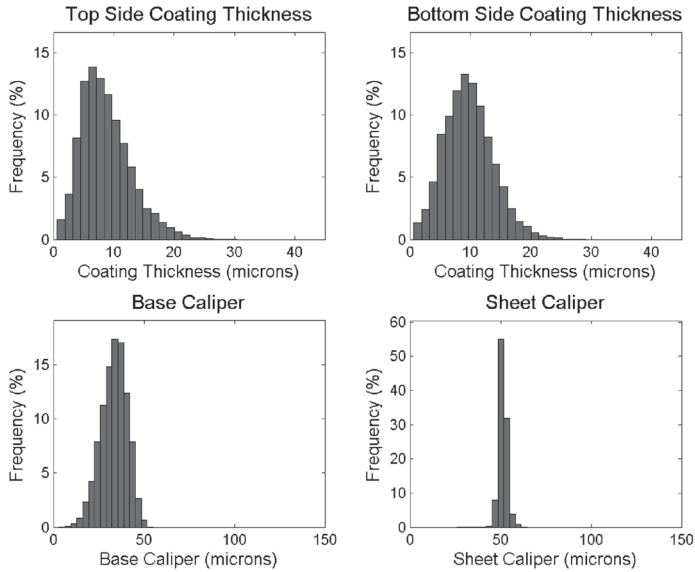


Figure 21 Results for calendered blade-coated sample.

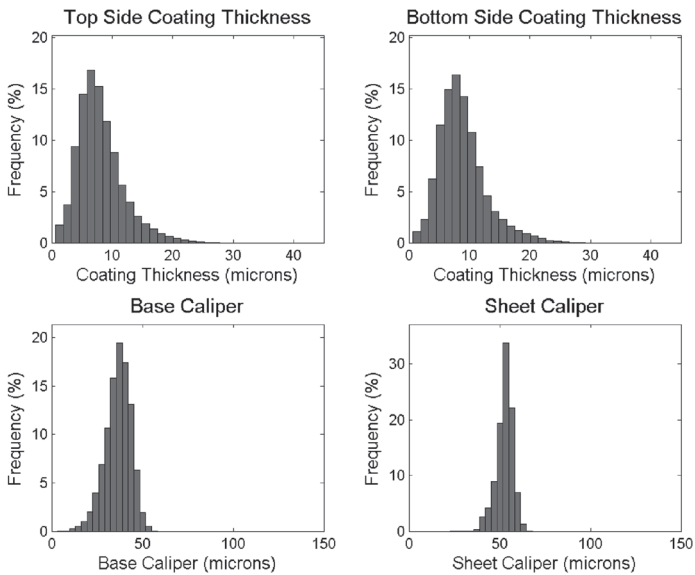


Figure 22 Results for calendered curtain-coated sample.

6 CONCLUSION

The presented concept of automated microtomy is a new approach to digitize paper structure in a comparatively fast way, analyzing all three dimensions with high resolution. The method offers the potential to digitize paper sample sizes in the order of magnitude of one square centimeter within hours. In addition the system allows resolutions of up to $0.26 \times 0.26 \times 0.50 \mu\text{m}^3$. This configuration opens a wide range of future research activities. In a first step image analysis methods were used to create detailed data about the spatial coating layer formation. The accuracy of spatial measurements performed on the generated data was validated with several other methods. That proves the correctness of the implemented sample digitization process and following image analysis.

7 OUTLOOK

Spatial coating layer analysis will be applied in conjunction with texture analysis algorithms to explore the correlation with various quality issues of coated papers. These issues are assumed to be closely related to non-uniformities in the coating layer, as for instance print and gloss mottle. Additional work will focus upon the influence of coating processes on base paper topography below the coating layer, since this information also is made available by the presented method.

The main focus in further developing the presented method will be on detailed analysis of the fiber network. Novel image analysis methods will allow the detection of single fibers in the network and their tracking through the 3D paper structure. Figure 23 shows an initial segmented fiber.

The possibility of accessing single fibers, and determining their position and orientation within the paper sample, will, for example, allow the 3D analysis of fiber orientation, calculation of spatial mass-distribution and mechanical behavior of fibre networks or determination of bonding areas between fibers. Also additional insights into the morphology of fibres in a paper sheet might be obtained.

An advantage of light microscopy is the capability to detect colors, see Figure 24. Based on these color images the three dimensional penetration behavior of different printing inks into the paper substrate will be studied.

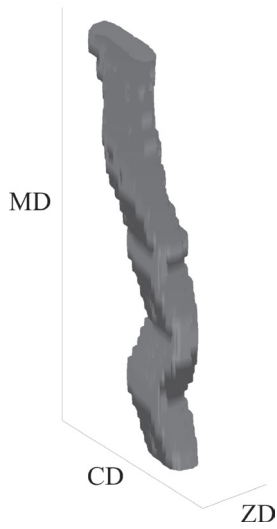


Figure 23 Cut-out of a segmented fiber (200 μm length).

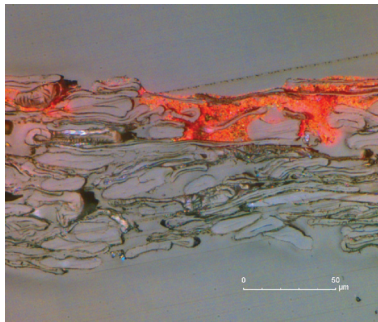


Figure 24 Flexo printed kraft paper.

ACKNOWLEDGEMENTS

The authors gratefully acknowledge financial support of Austrian Research Promotion Agency Ltd. (FFG) and from Mondi Business Paper Austria, Mondi Packaging Frantschach, M-Real Hallein, Norske Skog Bruck GmbH, Sappi Gratkorn GmbH, SCA Graphic Laakirchen AG, UPM Steyermühl and Voith Paper.

We also acknowledge the support of the Research and Development Department of IMERYS Minerals Ltd. in the validation of our method.

NOTATION

Symbol	Description
CD	cross direction
MD	machine direction
ZD	z direction through paper thickness
x	scalar value
$f(x)$	function of a scalar argument
\mathbf{x}	boldface is used for vectors and matrices
$f(\mathbf{x})$	function of a vector argument
$\ln(x)$	logarithm base e or natural logarithm of x
μ	mean or average value
σ	variance
Σ	covariance matrix
$N(\mu, \sigma)$	normal distribution with mean μ and variance σ
$N(\boldsymbol{\mu}, \boldsymbol{\Sigma})$	multivariate normal distribution with mean $\boldsymbol{\mu}$ and co-variance matrix $\boldsymbol{\Sigma}$
\mathbf{x}'	transpose of vector \mathbf{x}
\mathbf{A}^{-1}	inverse of matrix \mathbf{A}
$\varepsilon(\cdot)$	expected value
$p(\cdot)$	probability density
$P(\cdot)$	probability mass
$P(a, b)$	joint probability – probability of having both a and b
$p(a, b)$	joint probability density – probability of having both a and b
$\sum_{i=1}^n x_i$	sum from $i = 1$ to n – that is, $x_1 + x_2 + \dots + x_n$
$\int_a^b f(x)dx$	integral of $f(x)$ between a and b
$I(x, y)$	image with coordinates x and y

REFERENCES

1. E. Retulainen, K. Niskanen, and N. Nilsen. Fibers and bonds. In K. Niskanen, editor, *Paper physics*, Papermaking Science and Technology, page 59. Fapet Oy, 1998. book 16.
2. P.C. Cheng, W.L. Wu, T.H. Lin, and J.L. Wu, editors. *Multidimensional Microscopy*. Springer Verlag New York, 1994.
3. H. Nanko and J. Ohsawa. Mechanisms of fibre bond formation. In C.F. Baker and V.W. Punton, editors, *Fundamentals of Papermaking*, Transactions of the 9th Fundamental Research Symposium, pages 783–830. The Pulp and Paper Fundamental Research Society, 1989.
4. P.A. Moss, E. Retulainen, H. Paulapuro, and P. Aaltonen. Taking a new look at pulp and paper: Applications of confocal laser scanning microscopy (CLSM) to pulp and paper research. *Paperi ja Puu*, 75(1–2):74–79, 1993.
5. P.G. Auran. Surface structure analysis of paper based on confocal laser scanning microscopy (CLSM) imaging: aiming at the prediction of printability for wood-containing paper. In *Proceedings of SPIE – The International Society for Optical Engineering*, volume 3520, pages 161–169, 1998.
6. L. Xu, I. Parker, and Y. Filonenko. A new technique for determining fibre orientation distribution through paper. In *TAPPI International Paper Physics Conference*, pages 421–427, San Diego, USA, September 1999. Tappi Press Atlanta.
7. L. Xu, I. Parker, and C. Osborne. Technique for determining the fibre distribution in the z-direction using confocal microscopy and image analysis. *Appita Journal*, 50(4):325–328, July 1997.
8. E.J. Samuelson, Ø.W. Gregersen, P.J. Houen, T. Helle, C. Raven, and A. Snigirev. Three-dimensional imaging of paper by use of synchrotron x-ray microtomography. *Journal of Pulp and Paper Science*, 27(2):50–53, February 2001.
9. E.J. Samuelson, P.J. Houen, Ø.W. Gregersen, T. Helle, and C. Raven. Three-dimensional imaging of paper by use of synchrotron x-ray microtomography. In *TAPPI International Paper Physics Conference*, pages 307–312, San Diego, USA, September 1999. TAPPI Press Atlanta.
10. A. Goel, M. Tzanakakis, S. Huang, S. Ramaswamy, D. Choi, and B.V. Ramarao. Characterization of the three-dimensional structure of paper using x-ray microtomography. In *TAPPI Engineering Conference*, Atlanta, September 2000. TAPPI Press Atlanta.
11. S. Huang, A. Goel, S. Ramaswamy, B.V. Ramarao, and D. Choi. Transverse and in-plane pore-structure characterisation of paper. *Appita Journal*, 55(3): 230–234, May 2002.
12. S. Ramaswamy, S. Huang, A. Goel, A. Cooper, D. Choi, A. Bandyopadhyay, and B.V. Ramarao. The 3d structure of paper and its relationship to moisture transport in liquid and vapor forms. In C.F. Baker, editor, *The Science of Papermaking*, Transactions of the 12th Fundamental Research Symposium, pages 1289–1311. The Pulp and Paper Fundamental Research Society, 2001.
13. M. Gupta, A. Goel, S. Ramaswamy, H. Pande, and B.V. Ramarao. Analysis of z-directional 3d structural characteristics of commercial paper and hand sheets.

- In *Preprints of International Paper Physics Conference*, pages 85–88, Victoria, British Columbia, Canada, September 2003.
14. U. Aaltosalmi, M. Kataja, A. Koponen, J. Timonen, A. Goel, G. Lee, and S. Ramaswamy. Numerical analysis of fluid flow through fibrous porous materials. In *Preprints of International Paper Physics Conference*, pages 247–251, Victoria, British Columbia, Canada, September 2003.
 15. C. Antoine, P. Nygård, Ø.W. Gregersen, R. Holmstad, T. Weitkamp, and C. Rau. 3D images of paper obtained by phase-contrast X-ray microtomography: image quality and binarisation. *Nuclear Instruments and Methods in Physics Research A*, (490):392–402, 2002.
 16. C. Antoine, P. Nygård, R. Holmstad, Ø.W. Gregersen, T. Weitkamp, C. Rau, O. Sollheim, and P.J. Houen. Binarisation of 3D images of paper obtained by phase-contrast X-ray microtomography. In *Proceedings of the Final Workshop of COST Action E11: Characterization Methods for Fibres and Paper*, Espoo, Finland, 2001.
 17. C. Raven, A. Snigirev, I. Snigireva, P. Spanne, A. Souvorov, and V. Kohn. Phase-contrast microtomography with coherent high-energy synchrotron x rays. *Applied Physics Letters*, 69(13):1826–1828, September 1996.
 18. A. Snigirev, I. Snigireva, V. Kohn, S. Kuznetsov, and I. Schelekov. On the possibility of x-ray phase contrast microimaging by coherent high-energy synchrotron radiation. *Review of Scientific Instruments*, 66(12):5486–5492, December 1995.
 19. ESRF Beamline Handbook. European Synchrotron Radiation Facility, Grenoble. http://www.esrf.fr/exp_facilities/ID22/handbook.html, December 2004.
 20. R. Holmstad, C. Antoine, P. Nygård, and T. Helle. Quantification of the three-dimensional paper structure: Methods and potential. *Pulp & Paper Canada*, 104(7):47–50, July 2003.
 21. R. Holmstad, A. Goel, C.H. Arns, M.A. Knackstedt, and Ø.W. Gregersen. Effect of papermaking variables on the detailed 3D paper structure assessed by X-ray microtomography. In Ø.W. Gregersen, editor, *Proceedings of the 2004 Progress in Paper Physics Seminar*, pages 67–69, Trondheim, Norway, June 2004. NTNU, PFI and Tappi Paper Physics Committee.
 22. R. Holmstad, S. Ramaswamy, A. Goel, Ø.W. Gregersen, and B.V. Ramarao. Comparison of 3d structural characteristics of high and low resolution x-ray microtomographic images of paper and board. In *Preprints of International Paper Physics Conference*, pages 65–69, Victoria, British Columbia, Canada, September 2003.
 23. M.A. Knackstedt, C.H. Arns, R. Holmstad, C. Antoine, and Ø.W. Gregersen. Characterisation of 3D structure and transport properties of paper from tomographic images. In Ø.W. Gregersen, editor, *Proceedings of the 2004 Progress in Paper Physics Seminar*, pages 64–66, Trondheim, Norway, June 2004. NTNU, PFI and Tappi Paper Physics Committee.
 24. P. Bernada, S. Stenström, and S. Månson. Experimental study of the moisture distribution inside a pulp sheet using MRI. part I: Principles of the MRI technique. *Journal of Pulp and Paper Science*, 24(12):373–379, 1998.
 25. P. Bernada, S. Stenström, and S. Månson. Experimental study of the moisture

- distribution inside a pulp sheet using MRI. part II: Drying experiments. *Journal of Pulp and Paper Science*, 24(12):380–387, 1998.
26. S.G. Harding, D. Wessman, S. Stenström, and L. Kenne. Water transport during the drying of cardboard studied by nmr imaging and diffusion techniques. *Chemical Engineering Science*, 56(18):5269–5281, 2001.
 27. J. Leisen, B. Hojjatie, D.W. Coffin, S.A. Lavrykov, B.V. Ramarao, and H.W. Beckham. Through-plane diffusion of moisture in paper detected by magnetic resonance imaging. *Industrial & Engineering Chemistry Research*, 41(25):6555–6565, 2002.
 28. L. Nilsson, S. Månson, and S. Stenström. Measuring moisture gradients in cellulose fiber networks-an application of the magnetic-resonance-imaging method. *Journal of Pulp and Paper Science*, 22(2):48–52, 1996.
 29. M.J. Lehmann, E.H. Hardy, J. Meyer, and G. Kasper. Bestimmung der Faserstruktur und Packungsdichteverteilung in Tiefenfiltermedien mittels MRI. *Chemie Ingenieur Technik*, 75:1283–1286, September 2003.
 30. P. Blümler, B. Blümich, R. Botto, and E. Fukushima, editors. *Spatially resolved magnetic resonance – methods, materials, medicine, biology, rheology, geology, ecology, hardware*. Wiley-VCH Weinheim, Germany, 1998.
 31. A. Fenster and D.B. Downey. 3-D ultrasound imaging: A review. *IEEE Engineering in Medicine and Biology*, 15(6):41–51, 1996.
 32. E.P. Papadakis, editor. *Ultrasonic Instruments and Devices*. Academic Press San Diego, USA, 1999.
 33. U. Knotzer. *Image analysis evaluation of paper structure in z-direction*. PhD thesis, University of Technology Graz, 2002.
 34. U. Knotzer, M. Wiltsche, and H. Stark. Papierstruktur in z-Richtung. *Wochenblatt für Papierfabrikation*, 131(11–12):688–699, Juni 2003.
 35. U. Hirn. *New Methods in Paper Physics based on Digital Image Analysis*. PhD thesis, University of Technology Graz, 2005.
 36. U. Hirn, W. Bauer, and M. Wiltsche. Lokale Faserorientierung und ihr Einfluss auf kleinflächige Planlagestörungen. In H. Runge and R. Sangl, editors, *16th PTS-Symposium 2004 Chemical Technology of Papermaking*. PTS Munich, 2004.
 37. A.-L. Erkkilä, P. Pakarinen, and M. Odell. Sheet forming studies using layered orientation analysis. *Pulp & Paper Canada*, 99(1):81–85, 1998.
 38. M.H. Odell and P. Pakarinen. The complete fibre orientation control. In *XII. Valmet Paper Technology Days*, pages 20–41, Turku, Finland, June 2000.
 39. J.L. Thorpe. Exploring fiber orientation within copy paper. In *TAPPI International Paper Physics Conference*, pages 447–458, San Diego, USA, September 1999. Tappi Press Atlanta.
 40. J.D. Parker. *The Sheet-Forming Process*. Tappi, Atlanta, USA, 1972.
 41. C.-F. Yang, A.R.K. Eusufzai, R. Sankar, R.E. Mark, and R.W. Perkins Jr. Measurements of geometrical parameters of fiber networks. *Svensk Papperstidning*, (13):426–433, 1978.
 42. M. Hasuike, T. Kawasaki, and K. Murakami. Evaluation method of 3-d geometric structure of paper sheet. *Journal of Pulp and Paper Science*, 18(3):J114–J120, May 1992.

43. J. He, W.J. Batchelor, R. Markowski, and R.E. Johnston. A new approach for quantitative analysis of paper structure at the fibre level. *Appita Journal*, 56(5): 366–370, September 2003.
44. M. Aronsson. *On 3D Fibre Measurements of Digitized Paper*. PhD thesis, Swedish University of Agricultural Sciences Uppsala, 2002.
45. M. Hagen, R. Holen, R. Holmstad, and R. Blake. Digital identification of connected paper fibres with cracks. In Ø.W. Gregersen, editor, *Proceedings of the 2004 Progress in Paper Physics Seminar*, pages 164–166, Trondheim, Norway, June 2004. NTNU, PFI and Tappi Paper Physics Committee.
46. D. Capel and A. Zisserman. Automated mosaicing with super-resolution zoom. *Proc. IEEE Conf. on Computer Vision and Pattern Recognition*, pages 885–891, 1998.
47. R. Szeliski. Video mosaics for virtual environments. *IEEE Comput. Graphics Appl.*, 16(2):22–30, 1996.
48. R. Szeliski and J. Coughlan. Hierarchical spline based image-registration. *Proc. IEEE Conf. on Computer Vision and Pattern Recognition*, pages 194–201, 1994.
49. A. A. Efros and W. T. Freeman. Image quilting for texture synthesis and transfer. *Proceedings of SIGGRAPH*, pages 341–346, 2001.
50. L. G. Brown. A survey of image registration techniques. *ACM Computing Surveys*, 24(4):325–376, 1992.
51. C.D. Kuglin and D.C. Hines. The phase correlation image alignment method. *Proc. IEEE Int. Conf. Cybernet. Society*, pages 163–165, 1975.
52. H. Foroosh, J.B. Zerubia, and M. Berthod. Extension of phase correlation to subpixel registration. *IP*, 11(3):188–200, March 2002.
53. M. Donoser, M. Wiltsche, and H. Bischof. A new automated microtomy concept for 3d paper structure analysis. In *Proceedings of IAPR Conference on Machine Vision Applications – MVA*, Tsukuba, Japan, May 2005.
54. B. S. Reddy and B. N. Chatterji. An fft-based technique for translation rotation, and scale-invariant image registration. *IEEE Transactions on Image Processing*, Vol. 5(No. 8):1266–1271, 1996.
55. A. Levin, A. Zomet, S. Peleg, and Y. Weiss. Seamless image stitching in the gradient domain. *ECCV Proc.*, 2004.
56. D.L. Milgram. Computer methods for creating photomosaics. *IEEE Trans. Computer*, 23:1113–1119, 1975.
57. M. Uyttendaele, A. Eden, and R. Szeliski. Eliminating ghosting and exposure artifacts in image mosaics. *Conf. on Computer Vision and Pattern Recognition*, II:509–516, 2001.
58. E. H. Adelson, C. H. Anderson, J. R. Bergen, and P. J. Burt. Pyramid method in image processing. *RCA Engineer*, 29(6):33–41, 1984.
59. M. Sezgin and B. Sankur. Survey over image thresholding techniques and quantitative performance evaluation. *Journal of Electronic Imaging*, 13(1):146–165, January 2004.
60. A.l Bhattacharyya. On a measure of divergence between two statistical populations defined by their probability distributions. *Bulletin of the Calcutta Mathematical Society*, 35:99–110, 1943.

61. R.O. Duda, P.E. Hart, and D.G. Stork. *Pattern Classification*. Wiley-Interscience Publication, 2000.
62. P.J. Huber. *Robust Statistics*. John Wiley & Sons, New York, USA, 1981.
63. V. Barnett and T. Lewis. *Outlier in statistical Data*. John Wiley & Sons, 1994.
64. P.J. Rousseeuw and B.C. Van Zomeren. Unmasking multivariate outliers and leverage points. *Journal of the American Statistical Association*, 85(411):633–651, 1990.
65. P.J. Rousseeuw and K. Van Driessen. A fast algorithm for the minimum covariance determinant estimator. *Technometrics*, 41:212–223, 1998.
66. S. Mallat. *A Wavelet Tour of Signal Processing*. Academic Press, 1999.
67. S. Livens, P. Scheunders, G. Van de Wouwer, and D. Van Dyck. Wavelets for texture analysis, an overview. *Proc. ICIP and its Applications*, page 581–585, 1997.
68. B.B. Mandelbrot. *The Fractal Geometry of Nature*. 1968.
69. J. Levy Vehel, P. Mignot, and J.P. Berroir. Multifractals, texture, and image analysis. pages 661–664, 1992.
70. R.C. Gonzales, R.E. Woods, and S.L. Eddins. *Digital Image Processing with Matlab*. Prentice Hall, 2004.
71. M. Vogt, H. Praast, and L. Göttching. Charakterisierung der Rauheit von Papier mittels eines Lasersensors. *Das Papier*, 49(11):663–671, 1995.
72. H.J. Kent, N.A. Climpson, L. Coggon, J.J. Hooper, and P.A.C. Gane. Novel techniques for quantitative characterization of coating structure. *Tappi Journal*, 69(5):78–83, May 1986.

Transcription of Discussion

A NEW SLICE-BASED CONCEPT FOR 3D PAPER STRUCTURE ANALYSIS APPLIED TO SPATIAL COATING LAYER FORMATION

*Mario Wiltsche,¹ Michael Donoser,^{1,2} Wolfgang Bauer¹
and Horst Bischof²*

¹Institute for Paper, Pulp and Fiber Technology, Graz University of
Technology, Kopernikusgasse 24, 8010 Graz, Austria

²Institute for Computer Graphics and Vision, Graz University of
Technology, Inffeldgasse 16, 8010 Graz, Austria

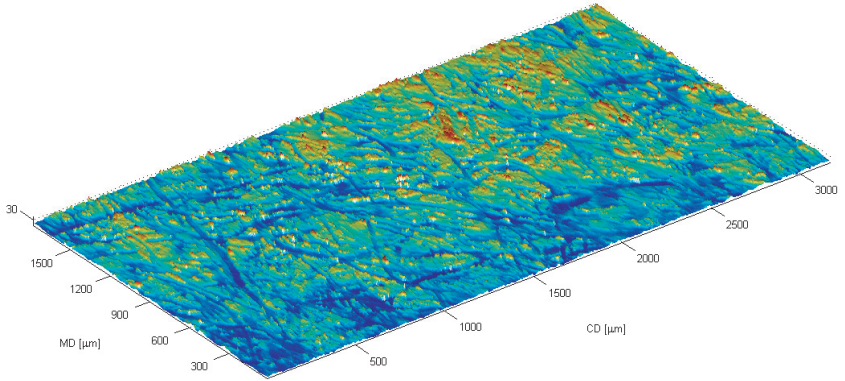
Additional material received from the authors to be included in the proceedings

The following two figures (on page 1504) show results for a woodfree coated, calendered sample.

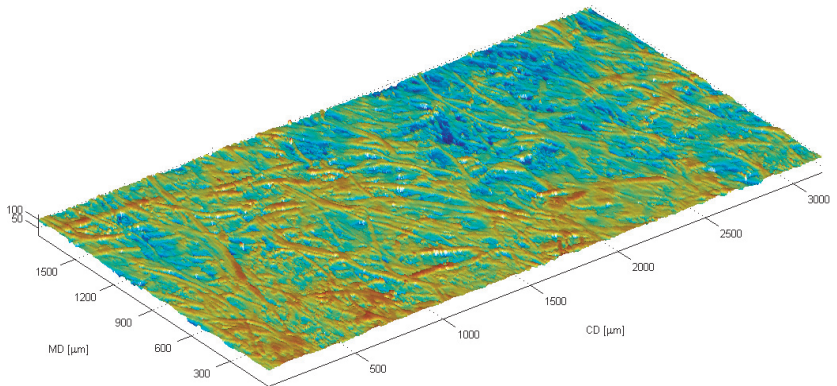
A 3D visualization of the local coating thickness is shown in the in the top figure. In the bottom figure the base paper topography under this coating layer is depicted.

It can clearly be seen, that fibers near the surface of the base paper, which can be identified in the base paper topography, cause impressions in the coating layer, thus affecting the local coating thickness. And on the other hand, local gaps in the basepaper surface cause increased values for the local coating thickness.

Discussion



Local coating thickness distribution.



Basepaper topography under this coating layer.

DISCUSSION CONTRIBUTIONS

Patrice Mangin U.Q.T.R./CIPP

Firstly, congratulations on the technique especially on how you differentiate pixels from the structure. Nevertheless, I have a question about the fine tuning of your segmentation technique. If I understand correctly, you actually have one representative pixel including RGB variations to represent the coating and you use distance statistics (Bhattacharyya) to find any other pixel which is either coating or not-coating. When looking at a continuous coating layer, I see no problem. Now for fine tuning, looking at statistical details, for instance a piece of coating material not in the continuous coating layer, or a small part of coating underneath the continuous coating layer, is the method that robust? Can we distinguish coating from what is not coating?

Mario Wiltsche

We have no restrictions regarding the shape of the coating layer. So the coating layer can be interrupted. There is no problem in analysis of, for instance, uncoated spots or penetrated coatings because the neighbourhood is analysed and, if there are many pixels around the analysed pixel where there is no coating, then the analysed pixel will be classified as a non-coating pixel. So the approach has no difficulties with things like that.

Patrice Mangin

So it is neighbourhood analyses which do the trick.

Christopher Dodson University of Manchester

A comment in connection with the last remark. The distance you used was the Bhattacharyya distance which is a very reasonable one. There is actually a rather more sensitive one, the Kullback-Leibler and it might worth trying that on your pixel distributions just to see if you have a better discrimination. If the delineation does not change then Bhattacharyya is good enough.

Mario Wiltsche

Okay. Thank you for the comment.

Discussion

Ho Fan Jang PAPRICAN

I just have couple of questions. The first one is: what is the imaging technique for generating those images?

Mario Wiltsche

Our system is equipped with a CCD camera. For illumination we use bright-field reflected light.

Ho Fan Jang

My second question is: what is the optical resolution of those images?

Mario Wiltsche

The optical resolution is $0.26 \mu\text{m}$. We use a 50 fold magnification which results in a pixel size of $0.26 \mu\text{m}$, so that is our limit for detection of microstructures.

Warren Batchelor Australian Pulp and Paper Institute

I was wondering how you avoid distorting the sample structure when you cut it.

Mario Wiltsche

There were similar approaches reported in the literature which were based on digitizing the cut section itself, but they are distorted or even broken. If you do the digitization on the surface of the block, a high accuracy between subsequent slice images is achieved. We do not have to correct any further displacements besides the vertical displacements between subsequent slice images. We just use image data, which were directly acquired on the cut surface without any further corrections and it works very well.

Steven Keller SUNY-ESF/ESPRI

A follow-up on that question on deformation: do you think your technique would be subject to the mechanical properties of the coating such as the brittleness or the elasticity?

Mario Wiltsche

I do not know that today but further research activities should be performed in order to get more information about the limitations of these techniques. We are just right on the beginning of working on this concept. I think the first results are quite promising.

Wolfgang Bauer Graz University of Technology

Just a comment on that. I think in general everything that you do on coating layers today is based on microtome sections of some sort. So I think the mistake we make by using this approach is the same as for any other method that we have for coating layer detection. Non-destructive approaches would, of course, be better but there is no method available that can be applied in day-to-day research.

Patrice Mangin U.Q.T.R./CIPP

You are using standard microscopy, could we apply the same idea with confocal microscopy? It would provide similar information with more reliability because of depth information. Is it feasible to adapt the technique to confocal microscopy?

Mario Wiltsche

That is a very good comment, but the problem is that we have the microscope fixed on the stage in order to cover a larger region of interest. Therefore, our custom built microscope has a very low weight, so when you use a confocal system, you have to move I think 20 or 30 kg with high accuracy to scan the block surface, so in this case the entire set-up would have to be redesigned. I think it would be good idea to do that, I think it would ensure more accuracy.

Øyvind Gregersen NTNU

I found this is a very neat method, but I would like to point out that it is also perfectly possible to study coating layers by SEM images of paper samples that are embedded in epoxy and polished. The benefit of the polishing technique compared to microtoming is that when you are cutting with a microtome, the blade will either go above or beneath each pigment particle. Whereas when you are grinding and polishing you are able to cut straight through each particle. This will give information in the SEM on the orienta-

Discussion

tion of each particle and the shape of each particle, if higher resolutions are used. However for 3D structures and for making analysing many samples quickly, I think you have done excellent work.

William Sampson

I have a question of my own, it is probably a little unfair because you probably have not done it, but I wondered if you had plotted the local thickness of the sheet against the thickness of the coating layers for all your positions, because you have done such nice work using multivariate distributions in processing your images? Your images will give you some nice multivariate distributions of data also.

Mario Wiltsche

We already did some of those correlations. I will present them at the TAPPI coating fundamental conference. We compared curtain coater and blade coater samples and we plotted, for example the base caliper under the coating versus top or bottom side coating thickness or total sheet caliper versus coating thickness values and so on, and we are able to distinguish these two applicators.